Effect of an artificial cavity on the microlayer and contact line dynamics during bubble growth in nucleate boiling

Cassiano Tecchio, Iacopo Regoli, Benjamin Cariteau, Gilbert Zalczer, Pere Roca I Cabarrocas, Pavel Bulkin, Jérôme Charliac, Simon Vassant, Vadim Nikolayev

Journal of Physics: Conference Series **2766** (2024) 012121 doi:10.1088/1742-6596/2766/1/012121

Effect of an artificial cavity on the microlayer and contact line dynamics during bubble growth in nucleate boiling

C Tecchio[1], I Regoli[1], B Cariteau[1], G Zalczer[2], P Roca i Cabarrocas[3], P Bulkin[3], J Charliac[3], S Vassant[2] and V S Nikolayev[2]

[1] Universit´e Paris-Saclay, CEA, STMF, 91191 Gif-sur-Yvette Cedex, France
[2] Universit´e Paris-Saclay, CEA, SPEC, CNRS, 91191 Gif-sur-Yvette Cedex, France
[3] Institut Polytechnique de Paris, Ecole Polytechnique, LPICM, CNRS, 91120 Palaiseau, France

E-mail: cassiano.tecchio@cea.fr

Abstract. We present an experimental study on the near-wall phenomena during the growth of a single bubble in saturated pool boiling of water at atmospheric pressure. Our focus is on the dynamics of triple contact line and liquid microlayer that can form between the heater and the liquid-vapor interface of the bubble. The microlayer thickness, the wall temperature distribution and the bubble shape are measured simultaneously and synchronously at 4000 fps by white light interferometry, infrared thermography and sidewise shadowgraphy, respectively. To study the effect of cavities (artificial nucleation sites) we compare two experiments using different heaters. In the first experiment, the bubble grows on a smooth surface of nanometric roughness whereas in the second, the bubble grows over a cylindrical cavity of 25 m diameter and 50 m depth. We found that the cavity reduces three times the required wall superheating to trigger the bubble growth. Moreover, the radii of the bubble, microlayer and dry spot are smaller by half and the macroscale bubble dynamics is also slower. The microlayer is thinner and is measurable in a larger portion of its extent. Based on the absence of interference fringes near the contact line (due to high interface slopes) and on recent numerical simulations, we conclude that the microlayer consists in two regions: a dewetting ridge near the contact line that grows over time and a flatter and wider region that thins over time. The microlayer can be seen as a film deposited by the receding meniscus and its profile is controlled by the viscous and surface tension effects; its thinning over time is due to local evaporation only. The ridge is a result of liquid accumulation due to contact line receding and strong viscous shear in the film.

1. Introduction

During the growth of bubbles on a heated wall, a thin layer of liquid having a thickness of a few m (known as microlayer) [1–5] can be formed between the wall and the liquid-vapor interface of the bubble (Fig. 1). The microlayer acts as a heat transfer bridge between the wall and the liquid-vapor interface of the bubble, promoting heat fluxes of the order of MW/m^2 that cool down the heater. A dry spot is also formed on the wall, establishing a triple liquid-vapor-solid contact line. Unlike the microlayer area, the wall heat flux is very low in the dry spot, resulting in a local rapid temperature increase. The use of artificial cavities in the investigations of boiling heat transfer is a very common practice [6–8] but the effect of them on the microlayer and

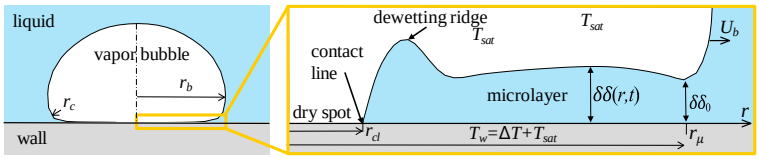

Figure 1. Schematics of the microlayer profile underneath the bubble.

contact line dynamics is still unclear. In this work, we report on the pool boiling experiments using the fast and synchronized shadowgraphy, white-light interferometry (WLI) and infra-red thermography (IRT) to reveal the effect of an artificial cavity on the microlayer and contact line dynamics.

2. Experiments

The experimental setup is schematized in Fig. 2. The boiling cell consists of a water pool surrounded by a temperature-regulated jacket. We use alternatively two boiling surfaces, each consisting of 950nm-thick indium-tin oxide (ITO) film deposited on magnesium fluoride (MgF_2) optical porthole using a radio-frequency magnetron sputtering system. In the first surface, no artificial cavity is present (Fig. 2a). The bubble nucleates on the ITO smooth surface of nanometric roughness. In the second, the bubble is nucleated over a cylindrical artificial cavity of 25 m diameter and 50 m depth (Fig. 2b). The cavity is produced on the MgF_2 surface by focused ion beam prior to the ITO deposition. MgF_2 is transparent to both visible and infrared (IR) light whereas ITO is transparent to visible but opaque to the IR waves. The experiment is performed at atmospheric pressure and at saturation conditions. The growth of a single bubble at a time is produced by heating up the ITO film locally with a 1.2 m wavelength IR continuous laser beam of 1.5 mm (no cavity) and 2.5 mm (cavity) diameters. The average applied heat fluxes are 1.1 MW/m^2 (no cavity) and 0.2 MW/m^2 (cavity).

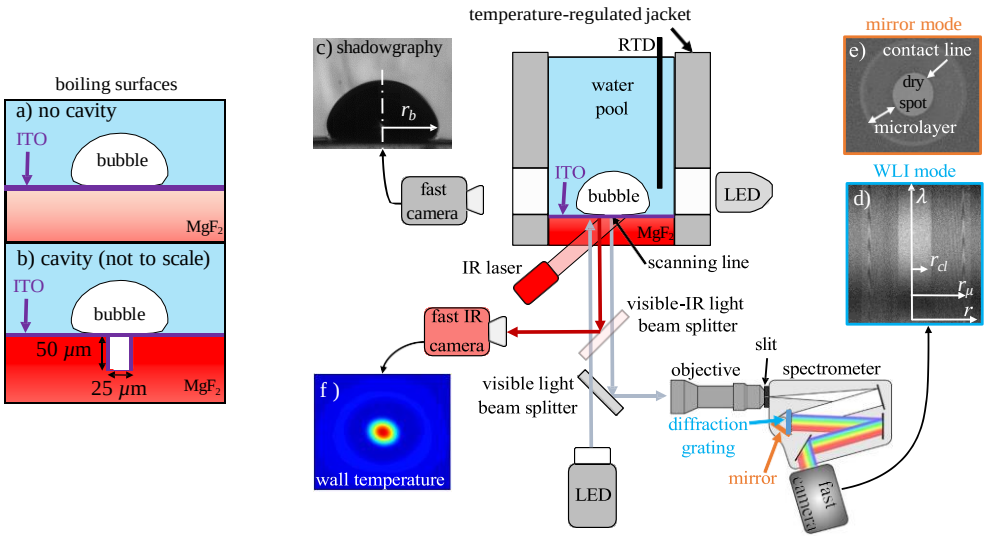

Figure 2. Schematics of the experimental setup.

High speed and high resolution optical techniques are employed to measure the near-wall features during the bubble growth. The bubble macroscopic shape (Fig. 2c) is observed by sidewise shadowgraphy with a spatial resolution of 32 m/px. The microlayer thickness is

measured by WLI. A LED light source produces a collimated beam of white light that is sent towards the bubble from below with perpendicular incidence to the heater. The light reflected at the interfaces MgF_2/ITO, ITO/microlayer and microlayer/vapor produces a colored fringe pattern directed towards a spectrometer with a visible light beam splitter. At the entrance of the spectrometer, a slit defines a scanning line on the heater. The setup is adjusted in such a way that the scanning line passes through the bubble center. The fringe pattern is then dispersed into wavelength λ by a diffraction grating inside the spectrometer, producing a spectral fringe map such as the one shown in Fig. 2d, in which the ordinate corresponds to λ and abscissa, to the physical position r on the heater along the scanning line. The microlayer thickness distribution $\delta(r)$ is determined by comparing the experimental spectral intensity with a two-beam interference model [9]. From Fig. 2d one can also obtain the dry spot (contact line) radius r_{cl} and the microlayer radius r_μ, within which the interference fringes appear. The diffraction grating can be replaced by a mirror to observe the dry spot and microlayer extents over the heater as shown in Fig. 2e. The wavelength bandwidth in WLI is 473 nm $\leq \lambda \leq$ 645 nm, and the spectral resolution is 0.16 nm/px. The WLI spatial resolution along r is 14 m/px.

The IRT technique is used to measure the temporal evolution of the wall temperature distribution $T_w(x, y, t)$. We use a custom-made multilayer visible-IR light beam splitter (transparent to visible but reflective to IR) positioned between the boiling cell and the visible light beam splitter to reflect the IR light emitted by the ITO. The reflected IR radiation is captured by a fast IR camera in the range 3-5 m. The recorded intensity is then related to temperature using a pixel-wise calibration [10]. The wall temperature is measured by a resistance temperature detector (RTD) with the water pool at thermal equilibrium. The spatial resolution of the IR camera is 84 m/px. All optical observations are recorded synchronously at 4000 fps. Calibration and validation of WLI and IRT are described in [9].

3. Theory

Schweikert et al. [11] hypothesized that the microlayer can be seen as the Landau-Levich film left behind the receding meniscus, cf. Fig. 1. This analogy is justified by the fact that the microlayer thickness is controlled only by the viscous and surface tension forces: the microlayer Reynolds number is tiny. The initial microlayer thickness (that without accounting for the evaporation) should thus be

$$\delta_0 = 1.34 r_c Ca^{2/3} \tag{1}$$

where r_c is the radius of curvature at the edge of bubble, cf. Fig. 1; the capillary number is $Ca = \mu U_b/\sigma$, with $U_b = dr_b/dt$ the speed of the receding meniscus at the bubble edge. The r_c value differs from the bubble radius r_b. The bubble foot is flattened by the inertial forces acting on the bubble downwards thanks to the rapid bubble growth. Therefore, the portion of bubble interface between the foot and the dome has a much larger curvature r_c^{-1} than that of the bubble dome, see Fig. 1; $\beta = r_c/r_b$ is thus expected to be much smaller than unity. This linear dependence of r_c holds for fast bubble growth because bubble profile remains self-similar. In the case of slow bubble growth, the changes in the bubble profile are more pronounced requiring a higher-order dependence in the form $r_c = \beta_0 r_b + \beta_1 r_b^2$. Values of r_b and U_b obtained from the experimental measurements are used in the calculation. To give the spatial dimension to δ_0, one mentions that the microlayer thickness at a point r corresponds to the time moment where $r_b = r$.

Microlayer can thin over time due to evaporation and radial liquid flow. Because of strong viscous stresses within the film, one can neglect the radial flow. By assuming a linear temperature distribution in the vertical direction and neglecting the heat flux towards the vapor, the energy balance in the microlayer reads

$$L\rho \frac{\partial \delta}{\partial t} = -k \frac{\Delta T}{\delta} \tag{2}$$

where L, ρ_l, and k_l stand for the latent heat, density and thermal conductivity of the liquid, respectively. $\Delta T = T_w - T_{sat}$ is the wall superheating with T_{sat} representing the saturation temperature, which is taken for the atmospheric pressure, and T_w the wall temperature obtained via IR thermography. To simplify the solution, one can use the weakness of both spatial and temporal ΔT variation along the microlayer; we thus use a constant value of ΔT . By integrating Eq. (2), one obtains the initial microlayer profile

$$\delta_0(r) = \sqrt{\delta(r)^2 + 2k_l \Delta T t_e/(L\rho_l)} \tag{3}$$

where t_e is the time of evaporation of microlayer at its point r.

4. Results

The time evolution of wall superheating ΔT at the nucleation point is shown in Fig. 3. The ΔT required to trigger the bubble nucleation is reduced by a factor of 3 with the cavity. This occurs because of a much larger amount of vapor is trapped inside the cavity. The boiling cycles follow a repetitive typical pattern of bubble nucleation, growth, detachment and waiting time. Therefore, one can analyze only one bubble growth period.

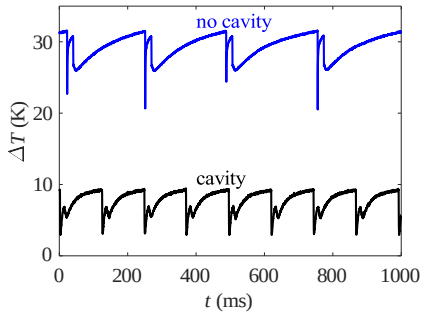

Figure 3. Effect of artificial cavity on ΔT at the nucleation point.

Figures 4 show the time evolution of bubble radius r_b, microlayer radius r_μ and dry spot r_{cl} without the artificial cavity and with the cavity. In both cases the microlayer exists. Its depletion occurs at t = 12.5 ms and t = 7 ms for the cases without the cavity and with cavity, respectively. With the cavity, all the three radii are reduced by a factor 2. This is because the inertial effects decrease with decreasing ΔT. Without the cavity (Fig. 4a), r_{cl} increases faster in the early stages between 0 ms $\leq t \leq$ 2 ms and then slows down until microlayer depletion, whereas with the cavity (Fig. 4b), r_{cl} evolves linearly from nucleation until microlayer depletion.

Figure 5 shows the time evolution of microlayer. In both cases the microlayer shows "bumped" profiles that thin over time due to evaporation. The geometry remains however unchanged because of quasi-absence of liquid flow. Only a portion of microlayer (far from the contact line) could be measured by WLI. This occurs because interference fringes are only detectable for microlayer slopes lower than $\approx 0.4^\circ$ [9]. We simulated the contact line motion numerically [12] for the no cavity case. The microlayer portion situated near the nucleation site is swept by the contact line receding [13]. Because of high viscous stresses in the film, the liquid cannot flow into the microlayer. Instead, it gets accumulated near the contact line thus creating there a dewetting ridge with high interfacial slopes as illustrated in Fig. 1. A similar ridge occurred in several recent DNS of nucleate pool boiling [1, 2, 4, 5].

The microlayer is thinner by a factor 3 in the case of the cavity, see Fig. 5. To understand this, we compare the theoretical and experimental δ_0. The theoretical is obtained with Eq. (1) by using the experimental values of r_b and U_b from Figs. 4 whereas the experimental δ_0 is given

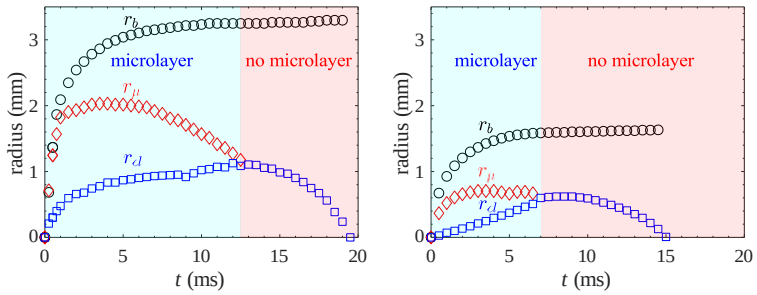

(a) With no cavity. (b) With a cavity.

Figure 4. Temporal evolution of bubble radius r_b, microlayer radius r_μ and dry spot (contact line) radius r_{cl}.

with Eq. (3) by using the $\delta(r)$ from Fig. 5. The obtained δ_0 values are plotted as a function of $r_b = r$ in Fig. 6; $\beta = 0.078$ and 0.156 are chosen to fit the experiment without cavity (fast bubble growth) and with cavity (slow bubble growth), respectively. During the bubble growth, U_b decreases whereas r_b increases, so a maximum occurs. Its position agrees with the experimental position, which validates the theoretical approach. One can now understand the thicker microlayer without cavity as a result of the faster bubble growth U_b, which promotes higher values of Ca during the receding meniscus at the bubble edge at very early stages ($Ca \approx 1 \times 10^{-2}$ without cavity and 4.5×10^{-3} with cavity). A larger Ca means a larger initial microlayer thickness.

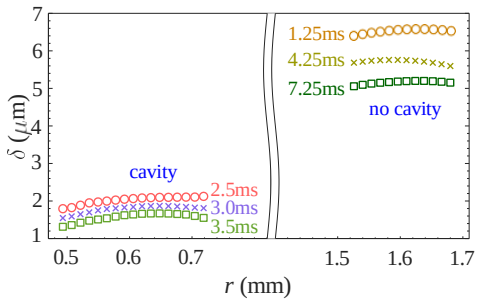

Figure 5. Experimental time evolution of microlayer thickness. Labels are the times since bubble inception.

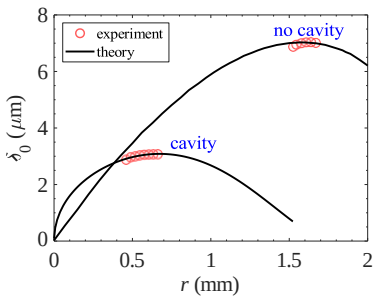

Figure 6. Theoretical (Eq. (1)) and experimental (Eq. (3)) initial microlayer thicknesses.

The effect of the cavity on the contact line motion can be observed in Fig.7. The capillary number $Ca_{cl} = \mu U_{cl}/\sigma$ of the contact line receding, with $U_{cl} = dr_{cl}/dt$, is plotted together with the wall superheating at the contact line $\Delta T_{cl} = T_{w,cl} - T_{sat}$ with $T_{w,cl}$ the wall temperature at the contact line. Ca_{cl} follows the same temporal decay as ΔT_{cl} in both cases (cavity and no cavity). This confirms that the contact line motion is controlled by the evaporation flux at the contact line, which is proportional to ΔT . In the no cavity case, the speed of the contact line receding [13] is therefore larger than in the cavity case as expected.

5. Conclusion

We perform an experimental study of single bubble growth at nucleate pool boiling in order to reveal the effects of a micrometric artificial cavity (nucleation site) on the microlayer and

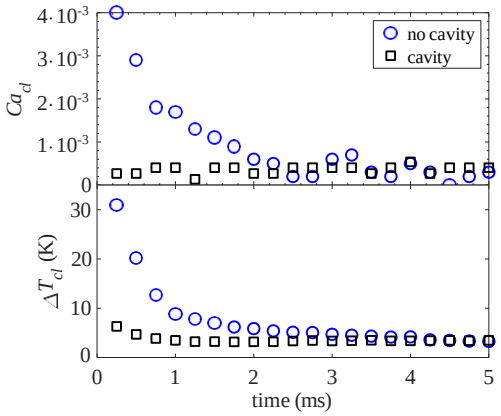

Figure 7. Effect of artificial cavity on the contact line.

contact line dynamics. We show that the use of an artificial cavity lowers the wall superheating required to nucleate the bubble, which reduces the inertial effects and produces a slower bubble growth. The bubble, microlayer and dry spot radii become two times smaller while the microlayer thickness is reduced by a factor 3 with the cavity. We show that the viscous and surface tension effects control the initial microlayer thickness while the contact line receding is driven by the wall superheating.

References

[1] Urbano A, Tanguy S, Huber G and Colin C 2018 *Int. J. Heat Mass Transf.* **123** 1128 – 1137

[2] Guion A, Afkhami S, Zaleski S and Buongiorno J 2018 *Int. J. Heat Mass Transf.* **127** 1271 – 1284

[3] Bureˇs L and Sato Y 2021 *J. Fluid Mech.* **916** A53

[4] Bureˇs L and Sato Y 2022 *J. Fluid Mech.* **933** A54

[5] Giustini G 2024 *Int. J. Multiphase Flow* **172** 104718

[6] Shoji M and Takagi Y 2001 *Int. J. Heat Mass Transf.* **44** 2763 – 2776

[7] Hutter C, Sanna A, Karayiannis T G, Kenning D B R, Nelson R A, Sefiane K and Walton A J 2013 *Exp. Therm. Fluid Sci.* **51** 94 – 102

[8] Voulgaropoulos V, Aguiar G M, Markides C N and Bucci M 2022 *Int. J. Heat Mass Transf.* **187** 122525

[9] Tecchio C 2022 *Experimental study of boiling: Characterization of near-wall phenomena and bubble dynamics* Ph.D. thesis Université Paris-Saclay

[10] Schweikert K, Sielaff A and Stephan P 2021 *Infrared Phys. Technol.* **118** 103862

[11] Schweikert K, Sielaff A and Stephan P 2019 *Int. J. Therm. Sci.* **145** 106025

[12] Tecchio C, Zhang X, Cariteau B, Zalczer G, Roca i Cabarrocas P, Bulkin P, Charliac J, Vassant S and Nikolayev V 2022 *Proc. 16th Int. Conf. Heat Transf. Fluid Mech. Thermodynamics (HEFAT-ATE 2022)* pp 624 – 629

[13] Zhang X and Nikolayev V S 2022 *J. Fluid Mech.* **948** A49